engineering proceedings

MDPI

Proceeding Paper

Industry 4.0: Correlation Analysis Applied to the Hot Stamping of AA7075 B-Pillars Pre-Assembled Using Friction Stir Welding †

Mohamad Idriss [1,*], Guillaume D'Amours [1], François Nadeau [1], Danick Gallant [1] and Ryan Myers [2]

[1] National Research Council Canada, Saguenay, QC G7H 8C3, Canada; guillaume.damours@cnrc-nrc.gc.ca (G.D.); francois.nadeau@cnrc-nrc.gc.ca (F.N.); danick.gallant@cnrc-nrc.gc.ca (D.G.)
[2] National Research Council Canada, London, ON N6G 4X8, Canada; ryan.myers@cnrc-nrc.gc.ca
* Correspondence: mohamad.idriss@cnrc-nrc.gc.ca
† Presented at the 15th International Aluminium Conference, Québec, QC, Canada, 11–13 October 2023.

Abstract: In this study, 220 AA7075-T6 B-pillars were fabricated using a thoroughly instrumented hot-stamping press under varied conditions. Feature engineering work identified nineteen attributes of the hot-stamping process as impacting four characteristics of the obtained B-pillars: electrical conductivity (%IACS), mechanical strength, distortion, and the presence of visible defects. Pearson correlation suggests an important correlation between the heating phase and the mechanical strength, as well as the %IACS values. As for distortion, the influence of the stamping phase is more obvious. Finally, no correlation was obtained between the hot stamping attributes and the presence of visible cracks. This is mainly due to the pre-assembly phase, i.e., Friction Stir Welding, which will be considered in future works.

Keywords: 7075 aluminum alloy; process chain; hot stamping; feature engineering; data analysis; Pearson correlation; Cyber Physical System (CPS)

Citation: Idriss, M.; D'Amours, G.; Nadeau, F.; Gallant, D.; Myers, R. Industry 4.0: Correlation Analysis Applied to the Hot Stamping of AA7075 B-Pillars Pre-Assembled Using Friction Stir Welding. *Eng. Proc.* **2023**, *43*, 15. https://doi.org/10.3390/engproc2023043015

Academic Editor: Mario Fafard

Published: 13 September 2023

1. Introduction

The majority of a vehicle's useful life cycle and greenhouse gas (GHG) emissions occur during the active use stage, accounting for between 84 and 91%, while the remainder occurs during production and end-of-life processing [1]. With such a large percentage of emissions occurring during useful life, significant investment has been made in studies on the impact of transitioning materials from high-strength steels (HSS) to aluminum or ultra-high-strength steel (UHSS) variants [2]. One of the primary challenges in the transition from steel-based components to aluminum comes in obtaining the structural properties required to still perform their functions at a reasonable cost while being resistant to critical wear and fatigue. For aluminum alloys to be considered for safety-critical components such as the B-pillar, they must possess relatively high yield strength and ductility. One of the candidates with the most potential at this level is 7075 aluminum alloy [3,4]. High-strength AA7075 is attractively positioned for these high-stress applications due to its strength-to-density ratio. NR. Harrison and SG. Luckey [5] demonstrated the feasibility of obtaining high levels of strength while hot stamping AA7075 sheets into an automotive B-pillar. F. Nadeau and NR. Harrison [6] provided an exploration into the generation of friction-stir welding for hot-stamping applications, showcasing the initial stages of development for combined processing of AA7075, demonstrating feasibility for automotive applications.

On another level, and within the framework of a new industrial revolution (Industry 4.0), new data-driven approaches are seeing light, seeking better process performance and increased agility, with less environmental impact. While some rely on extensive experimental testing [7] to optimize process parameters, others are based on high-volume

simulations [8]. Even though major advancements have been achieved based on these methods, some drawbacks are always present, e.g., pure numerical studies not validated with experimental data, specimens with simple geometry not being used in the production environment, or studies being based on nominal parameters without any consideration of their variation from the real process parameters. Nevertheless, all of these studies were conducted post mortem, and no real interaction has been established with the process during testing. This led to the introduction of the Cyber-Physical System (CPS) concept, which is the product of fully integrating computer science and digital systems with physical actuator and sensor systems to perform a series of operational tasks [9]. This includes high-speed data acquisition and data processing pipelines for monitoring the observable features and generating additional information features during component processing. Utilizing this automated data stream from the physical world, a digital twin of the physical component can be constructed [10]. This digital object makes it possible to run models to estimate performance at any given time. This information can be further leveraged for decision making and action in order to improve the efficiency of the production process. Ahmed et al. [11] demonstrated the effectiveness of a data-driven cyber-physical system for spot weldability using a five-layer approach.

In this study, a data-driven approach is applied for the hot stamping of a 2.0 mm thick AA7075 B-pillar, pre-assembled using friction stir welding (FSW). Butt-join FSW is utilized to investigate a singular scenario involving a uniform thickness (2 mm) and a single material (AA7075). While this pre-assembly step may appear redundant or unnecessary, it is important for readers to recognize that this study serves as an initial exploration for future investigations that will encompass various thicknesses and materials. This approach facilitates the customization of complex components to suit their intended applications by optimizing their properties accordingly. A total of 220 B-pillars were hot stamped, and the corresponding data were stored in a PostgreSQL relational database. Using a Python code, nineteen different forming attributes were extracted from the data collected for each formed specimen. On the other hand, four different characteristics/labels were assessed for each B-pillar, i.e., visible cracking, tensile strength, %IACS values, and distortion. Pearson correlation was then adopted to understand the influence of the extracted hot-stamping attributes on the corresponding labels. The results were then discussed based on the process fundamentals, and finally, conclusions were drawn. This study serves as a fundamental component in enhancing the instrumentation of the process and advancing the development of predictive machine learning models for seamless integration within a CPS environment.

2. Materials and Methods

2.1. Material

The studied material is 7075 aluminum alloy, which is well known in the aerospace industry. The corresponding chemical composition and mechanical properties are given in Tables 1 and 2, respectively. EBSD (Electron Backscatter Diffraction) analysis was performed on the material subsequent to annealing at various temperatures, namely, a minimum of 400 °C and a maximum of 470 °C. This temperature range is closely aligned with that typically employed in the hot-stamping process. The percentages of grains with a size smaller than 10 µm were found to be 87% and 86% for annealing temperatures of 400 °C and 470 °C, respectively. Notably, the investigated material exhibits a significant degree of grain size stability in response to changes in temperature, as depicted in Figure 1. The studied part is a 2 mm thick automotive structural component (a B-pillar, as presented below in Figure 2).

Table 1. Chemical composition (weight %) of the AA7075-T6.

Tested Material	Al	Zn	Mg	Cu	Cr	Fe	Si	Mn	Ti	Other
AA7075-T6	87.1–91.4	5.1–6.1	2.1–2.9	1.2–2.0	0.18–0.28	≤0.5	≤0.4	≤0.3	≤0.3	0.15

Table 2. Mechanical properties of the AA7075-T6.

Tested Material	Mechanical Properties			
	Young's Modulus (MPa)	Yield Strength Rp02% (MPa)	Max. Tensile Strength (MPa)	Maximum Elongation (%)
AA7075-T6	70,000	500	563	6.34

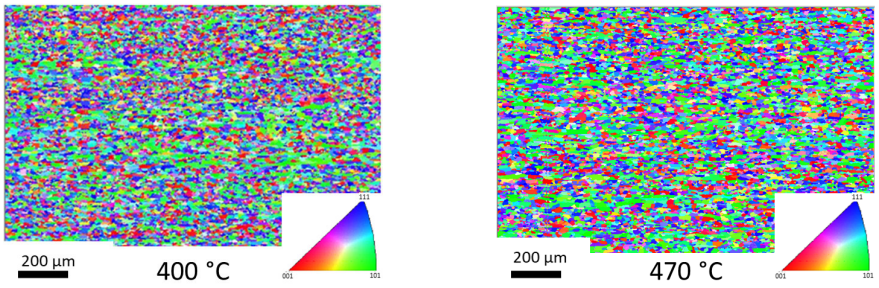

(**a**) (**b**)

Figure 1. EBSD maps obtained on AA7075 after annealing at (**a**) 400 °C and (**b**) 470 °C.

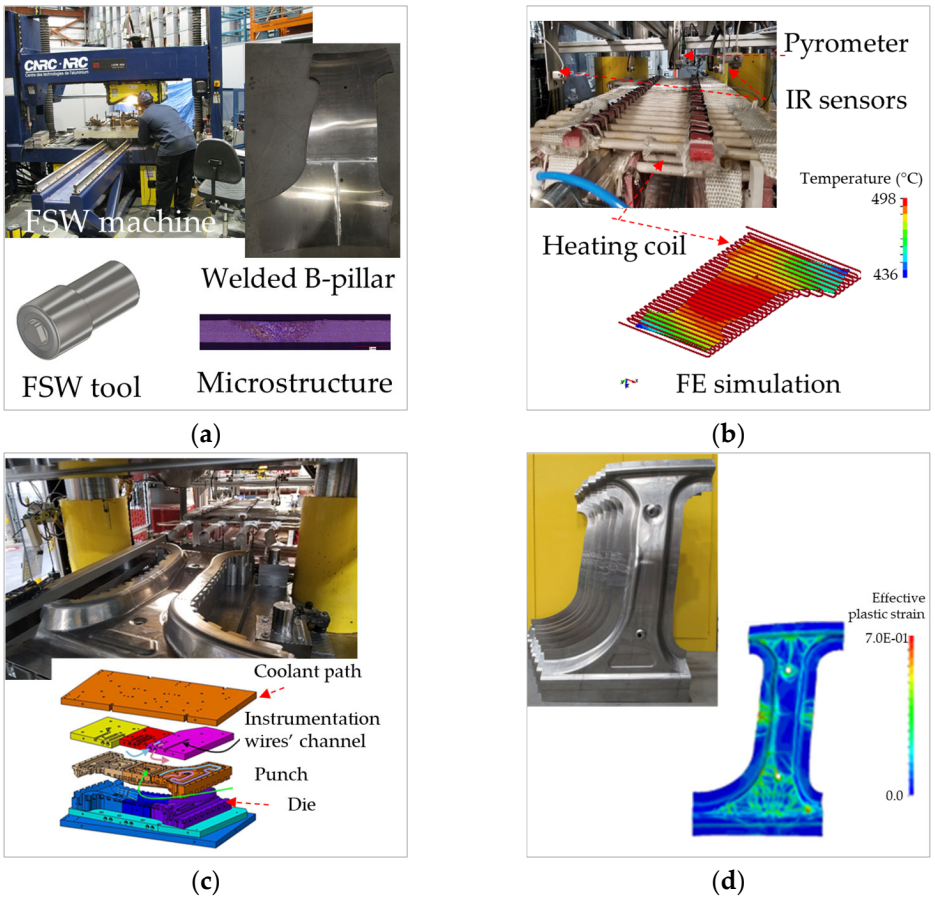

(**a**) (**b**) (**c**) (**d**)

Figure 2. (**a**) FSW joining process: the FSW machine, the FSW tool with a cup shoulder and a Triflat pin design, the welded B-pillar sheet, and an example of a weld microstructure. (**b**) Heating coil from the hot-stamping phase. (**c**) Hot-stamping press utilized to produce the B-pillars. (**d**) Final form of the obtained B-pillars with the corresponding FE result showing the distribution of the effective plastic strain.

2.2. Methods

2.2.1. Assembly Method: Friction Stir Welding (FSW)

Before manufacturing the B-pillar using friction stir welding (FSW), a development phase over 300 mm long specimens was performed in which various process parameters were compared. An MTS I-Stir PDS FSW machine was used in our experiments. The FSW tool shoulder diameters range from 8.5 mm to 12.5 mm, using a cup feature combined with a Triflat pin feature. The welding envelope is provided in Table 3, below, but the setting for each of the parameters is kept as proprietary information by the METALTec industrial group. The FSW parameters were developed to sustain the high-temperature formability required (≥420 °C) for the hot stamping process, which means targeting a competitive grain growth microstructure within the weld nugget [6]. Ultimately, one or two FSW butt-weld lines were produced on each B-pillar. These FSW weld lines were generated to maximize the number of extracted specimens on the bottom part of the B-pillar for further testing analysis (e.g., of stress corrosion cracking) (Figure 2).

Table 3. Adopted FSW parameter ranges for B-pillar assembly.

Rotational Speed (RPM)	Travel Speed (m/min)	Forging Force (kN)
500–1300	0.5–2.5	6.8–20.0

2.2.2. Transformation Method: Hot Stamping

The pre-assembled B-pillar is inserted in a copper-made heating coil for induction-type heat. The coil is a hollow cylinder with inner and outer diameters of 6.25 mm and 9.5 mm, respectively. From the outside, the coil is covered with refractory wool for security reasons, like avoiding overheating and short circuits due to any accidental contact between the spirals. A cooling liquid circulates in the inner part of the spirals. Using LS-DYNA, iterative FE analyses were conducted to achieve a relatively homogeneous heating distribution within the B-pillar (Figure 2b). After the heating phase is completed, a robotic hand transports the solution heat-treated sheet to the die within seconds. A hydraulic press with a maximum capacity of 1000 tons is utilized. A Condat soap diluted with water is automatically sprayed in the die for lubrification purposes. The die is kept at room temperature, ranging from 20 to 30 °C. The stamping phase is then started in order to obtain the final desired form. The obtained sheet is then removed from the die, cleaned with water, and finally undergoes classical artificial aging of 120 °C for 24 h (Figure 2c).

A total of 220 B-pillars were prepared within the framework of this project (Figure 2d). The hot-stamping envelope is provided in Table 4, below, but the setting for each of the individual parameters is kept as proprietary information by the NRC METALTec industrial group. The hot-stamping envelope contains a large set of recipes, leading to pass or fail B-pillars.

Table 4. Adopted hot-stamping parameter ranges for B-pillar forming.

Temperature Setpoint (°C)	Total Solution Heat Treatment Period (min)	Transfer Speed (mm/s)	Forming Speed (mm/s)	Intensification Pressure Rate (kN/s)	Quench Time (s)
410–495	7–10	72–700	45–150	375–3000	1–10

2.2.3. Instrumentation and Data Extraction

Both the assembly and the forming processes were thoroughly instrumented and studied. However, for the rest of this study, only the hot-stamping process will be considered. During the heating phase, a central multi-wave pyrometer is used to control the temperature of the heated sheet based on the set temperature point. In addition, five infrared sensors are positioned above the four corners of the B-pillar and in the center to follow the temperature variations of the sheet in real time. Similarly, during the stamping phase, all forming parameters are recorded in real time. This includes, for example, the lubricant

pressure and the die displacement variation with time, the linear actuator position and speed, the adopted recipe containing all the nominal values, etc. For each hot-stamped B-pillar, the recorded data are sent to a PostgreSQL relational database through two main channels: the first concerns the constant and nominal values that are extracted and sent to the database through the Ignition SCADA platform. Secondly, the real-time parameters are recorded in a TDMS file created by a National Instrument LabVIEW application. A Python script was prepared to detect the created TDMS file after the hot stamping of part, and then extract the corresponding data and organize it in a relational database.

3. Results

3.1. Attribute Extraction

Three main curves were obtained after each hot-stamping step: heating temperature (°C) vs. time (s), punch displacement (mm) vs. time (s), and punch load (kN) vs. time (s) (Figure 3a–c, respectively). In the next step, a Python script was prepared to extract the punch speed (mm/s) vs. time (s) curve from the punch displacement (mm) vs. time (s) curve (Figure 3d). From these four curves and for each hot-stamped B-pillar, nineteen independent forming attributes (presented in Figure 3 and explained in Table 5) were extracted using a feature engineering approach with the same Python script. This work was repeated for all 220 hot-stamped B-pillars, and the values of the corresponding attributes were stored in the database.

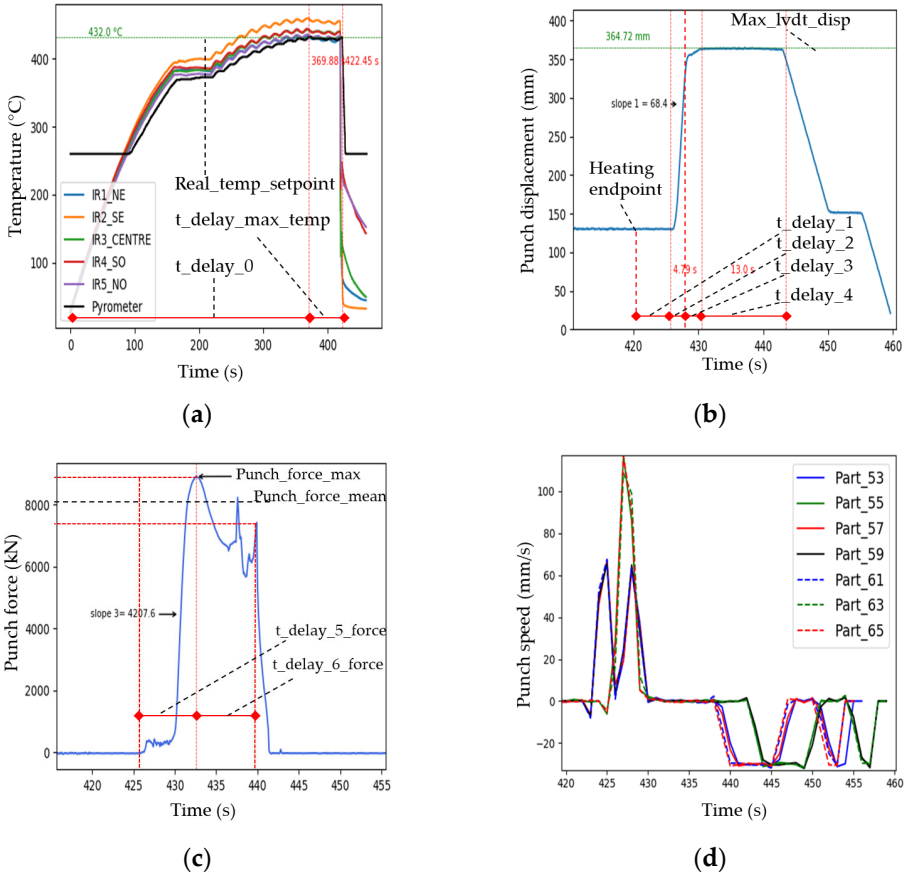

Figure 3. (**a**) Temperature vs. time curves: one corresponds to the pyrometer heating curve (black) and the other five correspond to the curves obtained with infrared sensors; (**b**) punch displacement (mm) vs. time (s) curve; (**c**) example of a punch force (kN) vs. time (s) curve; and (**d**) examples of punch speed(s) vs. time (s) curves.

Table 5. Hot-stamping attributes extracted from the corresponding forming curves.

Attribute Number	Attribute Name	Description	Parent Curve:
1	Real_temp_setpoint	Maximum temperature (°C) recorded by pyrometer	Temperature (°C) vs. time (s) curve: attributes 1 to 8
2	t_delay_0	Total duration (s) needed to attain maximum temperature	
3	t_delay_max_temp	Duration (s) at maximum temperature	
4	delta_temp_ir1	Difference (°C) between the reading of the pyrometer and the reading of the first infrared sensor at maximum temperature	
5 to 8	delta_temp_ir(2 to 5)	Same as delta_temp_ir1 but with sensors 2 to 5	
9	Max_lvdt_disp	Maximum punch displacement	Punch displacement (mm) to time (s): attributes 9 to 14
10	Slope 1	Displacement slope corresponding to punch speed (mm/s)	
11	t_delay_1	Delay (s) between the end of the heating phase and the start of the stamping phase	
12	t_delay_2	Delay (s) between the start of the punch displacement and the start of the transition phase: phase for forming the specimen curvatures	
13	t_delay_3	Duration (s) of the transition phase	
14	t_delay_4	Delay (s) at maximum LVDT displacement corresponding to quenching time	
15	Slope 3	Pressure intensification slope (kN/s)	Punch force (kN) vs. time (s): attributes 15 to 19
16	Punch_force_max	Maximum punch force (kN)	
17	Punch_force_mean	Punch force mean value (kN) calculated between the first and last peaks (presented in Figure 3c)	
18	t_delay_5_force	Delay (s) from 0 to maximum pressure	
19	t_delay_6_force	Delay (s) between first and last force peaks	

3.2. Label Extraction

Four different criteria (labels) were identified for assessing the final state of the obtained B-pillars:

1. Visible cracking: the first assessment method is visual inspection to verify the presence or not of cracks or necking in the B-pillar. This is expressed with a Boolean value in the database: 0 for no cracks and/or necking and 1 for the presence of at least one visible crack and/or necking (Figure 4a).
2. %IACS (International Annealed Copper Standard) values measured at four different positions of the B-pillar: %IACS corresponds to the percentage of conductivity the specimen has relative to annealed copper (considered 100% conductive). %IACS is a fast non-destructive method that provides information on the final mechanical resistance of the studied specimen. In the presented hot-stamping application, %IACS values were measured before and after the artificial aging step. The corresponding measurements are denoted as iacs_before and iacs_after, respectively (Figure 4a).
3. Tensile testing: for each of the obtained B-pillars, subsize tensile specimens are cut and tested following the ASTM E8/E8M standard [12]. The corresponding stress–strain curves are then obtained, and thus, the yield strength (MPa) and ultimate tensile strength (MPa) are extracted (Figure 4a).
4. The last evaluation criterion is the distortion value. Distortion is measured manually at the lower edge of the B-pillar and corresponds to a geometrical anomaly due to the cooling phase (Figure 4b).

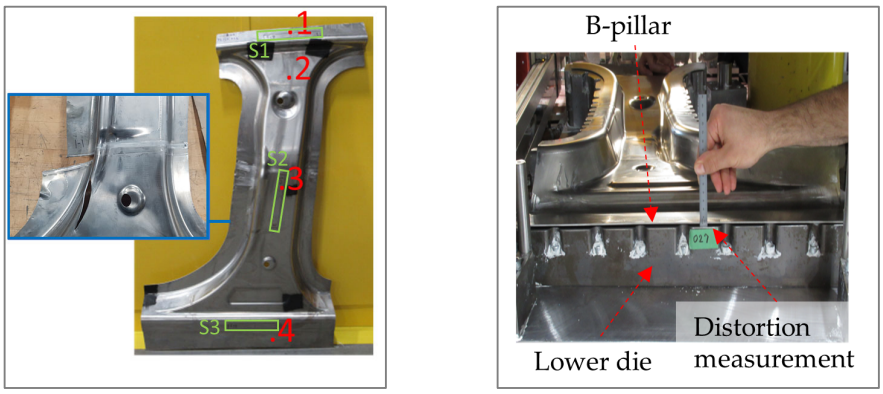

(**a**) (**b**)

Figure 4. (**a**) Hot-stamped B-pillar showing the positions of %IACS measurements (red dots 1, 2, 3, and 4) as well as the tensile specimens' extraction positions (green rectangles S1, S2, and S3). The image in the blue rectangle is an example of a visible crack; (**b**) example of a distortion measurement at the lower edge of the B-pillar.

3.3. Pearson Correlation

Pearson correlation refers to a statistical measure for determining the relationship between two quantitative variables and the degree to which they coincide with one another. For two given variables X and Y, the Pearson correlation is expressed as follows:

$$\rho(X,Y) = \frac{cov(X,Y)}{\sigma_X \sigma_Y} \quad (1)$$

where $cov(X,Y)$ is the covariance of X and Y, σ_X is the standard deviation of X, and σ_Y is the standard deviation of Y.

Using a Python script, the Pearson correlation is calculated between the attributes extracted for the 220 B-pillars (Section 3.1) and their corresponding labels (Section 3.2). The results are presented in the form of a heat map in Figure 5. In Figure 5, the cells with a star represent attributes that are strongly correlated with labels, where $|Pearson\ correlation\ value| \geq 0.65$.

Attributes \ Labels	iacs_before	iacs_after	distortion	crack	yield strength
t_delay_0	-0.024	-0.11	-0.042	-0.04	0.26
t_delay_1	0.019	0.094	0.045	0.06	0.086
t_delay_2	0.13	0.079	0.29	0.18	0.025
t_delay_3	0.086	0.083	★ 0.66	-0.29	-0.25
t_delay_4	-0.025	0.091	★ -0.7	0.042	-0.054
t_delay_5_force	0.2	0.3	-0.33	-0.26	-0.58
t_delay_6_force	-0.027	0.054	-0.054	-0.063	-0.083
t_delay_max_temp	0.55	0.63	-0.01	0.14	-0.16
real_temp_setpoint	★ -0.66	★ -0.7	0.12	0.2	★ 0.81
delta_temp_ir1_ne	-0.3	-0.43	0.19	-0.23	0.25
delta_temp_ir2_se	0.065	-0.097	0.27	-0.22	0.16
delta_temp_ir3_center	0.45	0.42	0.089	0.22	0.31
delta_temp_ir4_so	0.46	0.4	-0.095	0.091	0.37
delta_temp_ir5_no	0.47	0.42	-0.017	0.077	0.33
Slope 1	0.11	0.094	-0.13	0.023	-0.031
Slope 3	0.19	0.2	-0.43	0.3	0.03
max_lvdt_disp	0.016	0.1	★ -0.83	0.15	-0.055
punch_force_max	0.095	0.13	★ -0.7	0.2	-0.047
punch_force_mean	0.14	0.2	★ -0.8	0.18	-0.095

Scale: 1, 0.8, 0.6, 0.4, 0.2, 0, -0.2, -0.4, -0.6, -0.8, -1

Figure 5. Pearson correlation matrix between hot-stamping attributes and labels.

4. Discussion

From Figure 5, it can be seen that the yield strength is directly correlated with the heating temperature (Figure 6a). This can be explained by the DSC curve of the studied material, i.e., AA7075-T6 (Figure 6b). For temperatures between 420 °C (point D in Figure 6b) and 490 °C, the dissolution of the pre-existing hardening precipitates is partial. Therefore, in this range, the higher the heating temperature, the more complete the dissolution of the constituting hardening elements (Mg, Zn, Cu). This leads, after an artificial aging peak, to better-distributed precipitation, and thus, to better mechanical resistance in the obtained material.

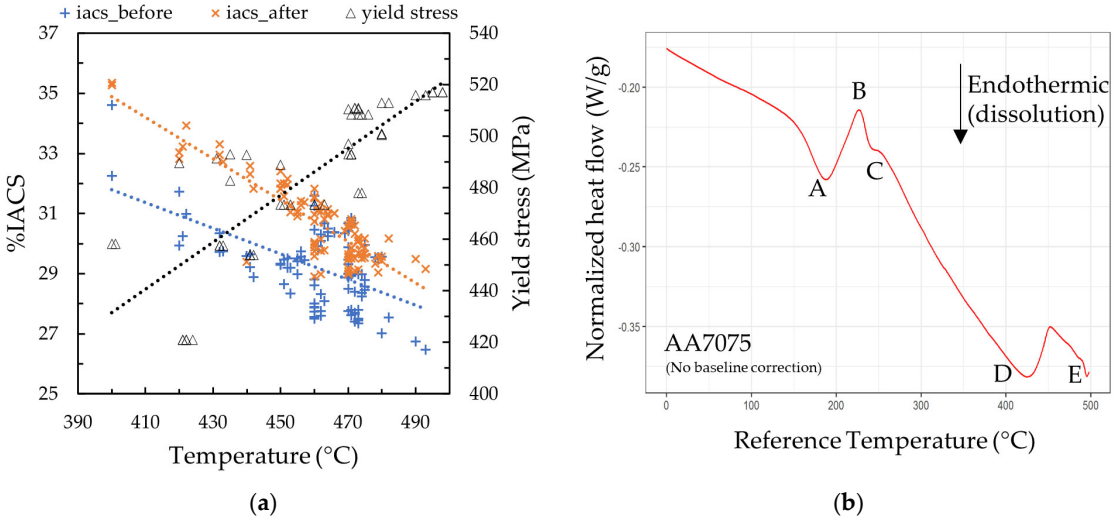

Figure 6. (**a**) 2D plot of the variations in the %IACS values (before and after artificial aging noted iacs_before and iacs_after, respectively) and yield stress (MPa) as a function of the heating temperature (°C). (**b**) DSC curve obtained for the AA7075-T6. Letters A to E represent exothermic and endothermic peaks/reactions corresponding to phases' creation and dissolution, respectively.

The %IACS values before and after artificial aging were mainly correlated with the maximum heating temperature (real_temp_setpoint). However, unlike yield strength, the higher the heating temperature, the lower the %IACS values (Figure 6a). For higher temperatures, there are more precipitates in the obtained material. These precipitates play a role as resisting elements in the conductivity of the material. This therefore leads to lower %IACS values. Finally, the influence of the aforementioned heating phase parameters on the %IACS values seems to be more important after artificial aging than before artificial aging. This is mainly due to the difference in temper stability: before artificial aging, the B-pillar is in an unstable W temper. After artificial aging, the B-pillar is in a T6 stable temper.

Distortion values are mainly correlated with five attributes: t_delay_3, t_delay_4, max_lvdt_disp, punch_force_mean, and punch_force_max (Figure 3 and Table 5). Aluminum is extremely prone to distortion [13]. As a general rule in hot stamping, the faster the forming process during quenching, the better the outcome. This is in total agreement with the obtained correlations regarding distortion. Higher t_delay_3 values correspond to lower-pressure intensification rates, and thus, to a slower stamping phase. This leads to an important cooling of the part while being formed. This leads to higher distortion values, as shown by the Pearson correlation (+0.66 from Figure 5). For max_lvdt_disp, punch_force_mean, and punch_force_max, it is important to note that these attributes are not completely independent. Higher punch displacement (max_lvdt_disp) leads to higher maximum punch force (punch_force_max), which leads to a higher mean punch force (punch_force_mean). This explains the same correlation trend obtained with the distortion (inverse proportionality). The higher the punch force value, the better the contact between the blank and the die, and the faster the forming phase compared to the quench rate, the lower the distortion value. Finally, higher values of t_delay_4, corresponding to

the quenching time, lead to lower distortion values. Aluminum has a relatively important linear expansion coefficient. This results in a relatively large expansion of aluminum during solution heat treatment and contraction during quenching. For higher values of t_delay_4, the part is constrained longer during quenching, resulting in a more controlled distortion value. However, after a certain quenching time threshold, this can lead to excessive residual stresses, which can be detrimental to the final piece shape. This is also true for the other observations, where it should be kept in mind that they were obtained within the nominal parameter ranges defined in Table 4. For example, the minimum heating temperature value tested was 410 °C, which is above the annealing temperature of the material. For lower temperature values, one should expect an increased influence of heating temperature on the distortion values.

Finally, there was no clear correlation between crack presence and the hot-stamping attributes. The cracks in the B-pillars were mainly identified in the welding zones: the fusion zone or the heat-affected zone. Therefore, for a better understanding of crack presence, the influence of the FSW attributes should be considered, which was outside the scope of this work.

5. Conclusions

In this work, a data-based approach was adopted to better understand the influence of hot-stamping inputs/attributes on the process outputs, i.e., the final characteristics of a prototype structural component typical of the automotive industry. 7075 aluminum alloy sheets with a thickness of 2.0 mm were friction stir welded, hot stamped, and subjected to different assembly and forming recipes to produce a total of 220 B-pillars. Pearson correlation was then adopted to study the influence of the process attributes, extracted using a feature engineering approach, on the corresponding outputs. On the basis of this, the following conclusions were drawn:

1. %IACS values and mechanical strength are influenced by the heating phase of the process. As proved by the DSC curve, the higher the heating temperature, the higher the dissolution during partial heat treatment, and the better distribution of the precipitates after the artificial aging step. This leads to higher precipitate cluster density, leading to greater resistance to the conductivity of the material (lower %IACS values) and more resistance to dislocation motion (higher mechanical resistance).
2. With the adopted heating temperature range (410 °C to 490 °C), the final distortion of the B-pillar was better correlated with the forming phase of the process. The faster the forming, the better the outcome. This translates into a decrease in the distortion value with decreasing transition forming time (t-delay-3). In addition, an increase in the punch force value leads to better forming conditions, and thus, to a decrease in the distortion values. Finally, a longer quenching time leads to greater shrinkage of the blank in the die during hot stamping, which explains the decrease in distortion values.
3. For a better understanding of the visible cracks, a similar correlation study will be conducted on the data extracted from the FSW process. This will lead to definition of the attributes that influence the whole described process chain. In the next step, machine learning models will be developed to predict, based on the identified FSW and hot-stamping attributes, the outcome of the process.

Finally, on the basis of the results of this study, two general points are to be considered. First, the correlation study helped introduce the concept of 'smart instrumentation' instead of 'extensive instrumentation'. As an example, in our case study, and during heating, the influence of the temperature gap between the center of the B-pillar and the four corners seems to be negligible in terms of the part outcome compared to other attributes. Second, the data-driven approach shows great potential in modernizing manufacturing environments. However, in these environments, data availability is limited by different factors, e.g., the ranges adopted, expensive or difficult instrumentation, and small datasets. The insight of process experts is still of crucial importance.

Author Contributions: Conceptualization, G.D., F.N. and D.G.; methodology: M.I., G.D., D.G. and F.N. software: M.I. and R.M.; validation: G.D. and F.N.; formal analysis: M.I., G.D. and F.N.; writing: M.I. and R.M.; writing—review and editing: M.I., F.N. and R.M. All authors have read and agreed to the published version of the manuscript.

Funding: This research was funded by the Canadian Office for Energy Research and Development (OERD), grant number NRC-20-19.

Institutional Review Board Statement: Not applicable.

Informed Consent Statement: Not applicable.

Data Availability Statement: The data that have been created and used in this study are confidential and are kept as proprietary information by the METALTec industrial group.

Acknowledgments: The authors acknowledge the contributions of the NRC team, who participated in the various technical and administrative aspects of this studyas well as the METALTec industrial research group members who supported this research work and publication. Special thanks are extended to Philippe Tremblay, without whom this work could not have been completed.

Conflicts of Interest: The authors declare no conflict of interest. The funders had no role in the design of the study; in the collection, analyses, or interpretation of data; or the writing of the manuscript. However, they gave their consent so this part of the results could be published.

References

1. Lewis, A.M.; Kelly, J.C.; Keoleian, G.A. Vehicle lightweighting vs. electrification: Life cycle energy and GHG emissions results for diverse powertrain vehicles. *Appl. Energy* **2014**, *126*, 13–20. [CrossRef]
2. Mass Reduction for Light-Duty Vehicles for Model Years 2017–2025: Peer Review Summary Report | NHTSA. Available online: https://www.nhtsa.gov/document/mass-reduction-light-duty-vehicles-model-years-2017-2025-peer-review-summary-report (accessed on 14 May 2023).
3. Wang, N.; Ilinich, A.; Chen, M.; Luckey, G.; D'Amours, G. A comparison study on forming limit prediction methods for hot stamping of 7075 aluminum sheet. *Int. J. Mech. Sci.* **2019**, *151*, 444–460. [CrossRef]
4. Hui, W.; Luo, Y.; Friedman, P.; Chen, M.; Lin, G.A.O. Warm forming behavior of high strength aluminum alloy AA7075. *Trans. Nonferrous Met. Soc. China* **2012**, *22*, 1–7.
5. Harrison, N.R.; Luckey, S.G. Hot stamping of a B-pillar outer from high strength aluminum sheet AA7075. *SAE Int. J. Mater. Manuf.* **2014**, *7*, 567–573. [CrossRef]
6. Nadeau, F.; Harrison, N.R. Friction Stir Welding Process Development of AA7075 for Hot Stamping Applications. In *Friction Stir Welding and Processing IX*; Springer: Berlin/Heidelberg, Germany, 2017; pp. 197–209.
7. Farzadi, A.; Bahmani, M.; Haghshenas, D.F. Optimization of operational parameters in friction stir welding of AA7075-T6 aluminum alloy using response surface method. *Arab. J. Sci. Eng.* **2017**, *42*, 4905–4916. [CrossRef]
8. Xiao, W.; Cai, H.; Lu, W.; Li, Y.; Zheng, K.; Wu, Y. Multi-objective optimization with automatic simulation for partition temperature control in aluminum hot stamping process. *Struct. Multidiscip. Optim.* **2022**, *65*, 84. [CrossRef]
9. Uhlemann, T.H.-J.; Lehmann, C.; Steinhilper, R. The digital twin: Realizing the cyber-physical production system for industry 4.0. *Procedia CIRP* **2017**, *61*, 335–340. [CrossRef]
10. Fuller, A.; Fan, Z.; Day, C.; Barlow, C. Digital twin: Enabling technologies, challenges and open research. *IEEE Access* **2020**, *8*, 108952–108971. [CrossRef]
11. Ahmed, F.; Jannat, N.-E.; Schmidt, D.; Kim, K.-Y. Data-driven cyber-physical system framework for connected resistance spot welding weldability certification. *Robot. Comput. Integr. Manuf.* **2021**, *67*, 102036. [CrossRef]
12. Standard Test Methods for Tension Testing of Metallic Materials. Available online: https://www.astm.org/e0008_e0008m-22.html (accessed on 15 May 2023).
13. MacKenzie, D.S. Heat treating aluminum for aerospace applications. *Heat Treat. Prog.* **2005**, *5*, 37–43.